

SOFT ROBOTS

Controlling subterranean forces enables a fast, steerable, burrowing soft robot

Nicholas D. Naclerio^{1*}, Andras Karsai², Mason Murray-Cooper², Yasemin Ozkan-Aydin², Enes Aydin², Daniel I. Goldman², Elliot W. Hawkes¹

Copyright © 2021
The Authors, some
rights reserved;
exclusive licensee
American Association
for the Advancement
of Science. No claim
to original U.S.
Government Works

Robotic navigation on land, through air, and in water is well researched; numerous robots have successfully demonstrated motion in these environments. However, one frontier for robotic locomotion remains largely unexplored—below ground. Subterranean navigation is simply hard to do, in part because the interaction forces of underground motion are higher than in air or water by orders of magnitude and because we lack for these interactions a robust fundamental physics understanding. We present and test three hypotheses, derived from biological observation and the physics of granular intrusion, and use the results to inform the design of our burrowing robot. These results reveal that (i) tip extension reduces total drag by an amount equal to the skin drag of the body, (ii) granular aeration via tip-based airflow reduces drag with a nonlinear dependence on depth and flow angle, and (iii) variation of the angle of the tip-based flow has a nonmonotonic effect on lift in granular media. Informed by these results, we realize a steerable, root-like soft robot that controls subterranean lift and drag forces to burrow faster than previous approaches by over an order of magnitude and does so through real sand. We also demonstrate that the robot can modulate its pullout force by an order of magnitude and control its direction of motion in both the horizontal and vertical planes to navigate around subterranean obstacles. Our results advance the understanding and capabilities of robotic subterranean locomotion.

INTRODUCTION

Robots are well suited for navigating extreme environments such as outer space, ocean floors, or disaster scenes where it is dangerous or expensive for humans to enter. Robots such as NASA's Mars Curiosity rover (1), Jason Jr.—the remotely operated vehicle that helped find the Titanic (2)—and TEPCO's series of robots for accessing the reactors of Fukushima (3) have contributed to scientific discovery, helped probe inaccessible locations, and captured the attention of the general public. Although many robots have been designed and built for these challenging environments, one underexamined extreme environment is the subterranean world. The focus of this work is locomotion through such an environment, in particular, directly through granular media where no paths or tunnels exist.

Our understanding of subterranean locomotion is relatively limited when compared with the study of movement through gas and liquid, which established formalized principles enabling effective airplanes and submarines more than 100 years ago. Theories from aerodynamics and hydrodynamics can help inform terradynamic locomotion (4), but the physics of locomotion through the ground are fundamentally different from those of movement in air or water. Not only are the resistive drag forces in soil and granular media orders of magnitude greater than in air or water (5), but also a different type of lift force is present that diverts a symmetric burrower from its course (Fig. 1A). We study these two challenges to advance the field of terradynamics and inform the design of a robot that can overcome them.

The first challenge of subterranean locomotion is the drag force that directly resists movement (Fig. 1A). We focus specifically on dry granular media or collections of solid particles whose strength

and normal resistive forces are created by frictional interactions without substantial cohesion, e.g., sand (6). The total drag force on a body in granular media can be computed via resistive force theory as the integral of normal and tangential forces caused by friction and pressure acting on it (4, 7). Because of gravity and friction, in a homogeneous granular medium, lithostatic pressure and yield strength increase linearly with depth (8, 9).

The second challenge is the interaction force that can divert a burrower from its intended course (Fig. 1A). This granular lift force is analogous to the lift force in fluids but is different in nature. The difference arises from the component of granular lift force that is caused by the gradient in lithostatic pressure, resulting in a yield strength gradient in the media. Because of this strength gradient, it is easier to push granular media up than it is to compact it down. Thus, the magnitude of the normal force acting on a deeper part of a moving object is higher than that acting on a shallower part, causing lift opposite to gravity. Therefore, symmetric objects moving horizontally through granular media experience a vertical lift force (9–11), causing some projectiles to “j-hook” upward after affecting granular media at an oblique angle (12) and burrowing robots to surface (13). At the same time, for objects moving vertically downward, this component of lift still opposes gravity, becoming aligned with the drag force.

To overcome these two challenges of granular drag and lift forces, most current burrowing methods rely on mechanisms enabled by large machines with stiff and massive components. Conventional methods such as auger drilling, hydraulic rotary drilling, and tunnel boring (14–17) effectively overcome these forces, but they are not ideal for small, minimally invasive, exploratory robots due to the heavy equipment required. Other mechanical burrowing methods have been proposed that would be more suitable for robots, including screw (18), reciprocating drill (19, 20), and hammer (21) mechanisms. An example robot application is NASA's Interior Exploration using Seismic Investigations, Geodesy and Heat Transport (InSight) mission, which used a hammering mechanism to drive a

¹Department of Mechanical Engineering, University of California, Santa Barbara, Santa Barbara, CA 93106, USA. ²School of Physics, Georgia Institute of Technology, Atlanta, GA 30332, USA.

*Corresponding author. Email: nnaclerio@ucsb.edu

temperature probe into the martian regolith. In laboratory testing, the device was able to burrow up to 5 m deep in 12 hours (22), but after 2 years on Mars, it was ineffective (23), illustrating the challenges

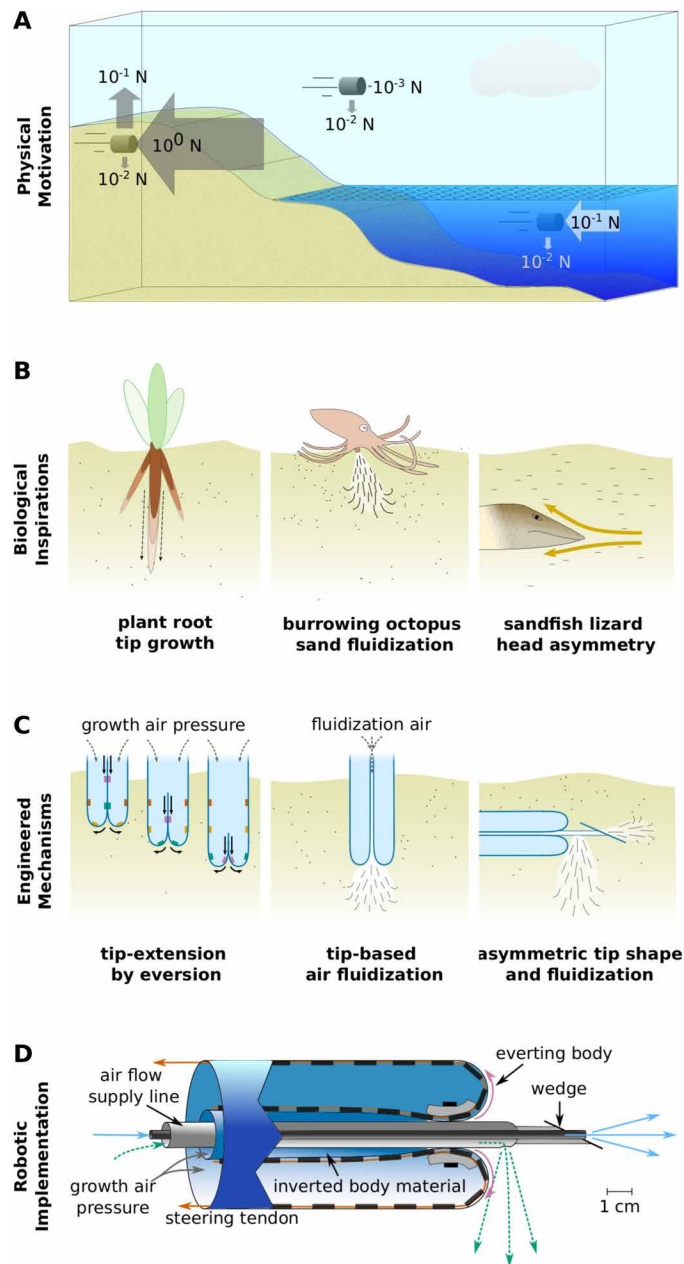


Fig. 1. Overview of the motivation, inspirations, mechanisms, and design of the soft burrowing robot. (A) The drag, lift, and net buoyancy forces on a 1-cm-diameter steel cylinder moving at 4 m/s through granular media are qualitatively different than in a gas or liquid. Its drag is orders of magnitude higher, and a symmetric object experiences lift. (B) The mechanisms of this robot are inspired by plant roots, various aquatic organisms, and burrowing reptiles. (C) The robot features three engineered mechanisms to improve burrowing: tip extension by eversion to reduce skin drag, tip-based aeration and fluidization to reduce resistive forces, and asymmetric tip shape and airflow direction to overcome lift. (D) The robot features an everting body (blue) with a constrictor ring to seal it against the tip-flow air supply line (gray) that delivers both forward and downward airflow to the tip, with steering tendons (orange) for tip-localized steering.

of robotic burrowing. Instead of trying to combat lift and drag forces directly, examples in living systems suggest an alternative: reduce and control the otherwise large subterranean interaction forces (Fig. 1B).

The first set of examples from nature uses tip extension, an effective method used by plant roots to burrow through soil (Fig. 1B, left). The mature, proximal region of a root can remain stationary relative to its surrounding while its apical tip extends, exerting more than 1 MPa of pressure (24–26), sloughing cells, and excreting mucus (27–29). Tip extension allows the roots of a wild fig tree *Ficus natalensis* to extend as deep as 120 m (30) and those of a single American aspen (*Populus tremuloides*) clone to cover 0.433 km² (31). Sadeghi, Mazzolai, and collaborators have pioneered tip-extending burrowing robots that “grow” by adding new material to their tips, realized either via additive manufacturing (32–34) or mechanically driven everting skins (35). Our group has pursued a pneumatically driven everting skin design (36, 37) due to its speed and simplicity.

Granular fluidization via the flow of fluid is another method found in effective burrowing organisms. Flow-based fluidization uses the pressure of an interstitial fluid passing through granular media to balance the gravitational force on the grains, suspending them in the fluid medium and allowing the particles to flow in shear (38). This reduces the medium’s yield strength and therefore the resistive force that it can exert on an object (39). Some burrowing organisms and their respective fluidization methods include the Pacific sandfish (*Trichodon trichodon*), which expels water from its gills (40); the mole crab (*Emerita*), which quickly rows its legs (38, 41); the southern sand octopus (*Octopus kaurna*), which expels a jet of water from its body (Fig. 1B, center) (42); and several clams (*Ensis*) that use the motion of their bodies and eject water from their shells (43, 44). The clams inspired two burrowing robots (45, 46), whereas a proposed lunar excavation method used a gas jet to excavate regolith in a manner similar to the octopus (47). Fluidization is also used to reduce forces in the construction industry, such as in pile jetting (48) and sonic drilling (49–51).

Last, asymmetries are used by burrowing animals to control lift, helping them maintain their course underground. Studies hypothesize that some desert-dwelling reptiles (52), such as the sandfish lizard (*Scincus scincus*) (Fig. 1B, right) (5, 53) and Western shovel-nosed snake (*Chionactis occipitalis*) (54), use the posture of their wedge-shaped heads to modulate lift while burrowing in sand. A downward-pointing nose may create negative lift to help diving, and an upward-pointing nose may create positive lift to aid in resurfacing. The effect of wedged-shaped tips has been demonstrated to affect both lift (5) and horizontal steering (55) for robots burrowing in dry granular media.

Given the observed biological mechanisms of tip extension, granular fluidization, and tip asymmetries, as well as an understanding of resistive force theory, we form three hypotheses about the control of interaction forces on objects moving in granular media. Hypothesis 1: A tip-extending body will experience less drag force than an equally sized intruding body by an amount equal to its skin drag. Tip extension should reduce tangential forces along an object’s body because it eliminates relative motion with respect to the granular media; thus, only normal forces at the tip will contribute to drag in this case. Hypothesis 2: When tip-based airflow aerates or fluidizes the local media in front of a moving object, the drag force on the object will reduce by an amount proportional to the magnitude of the component of flow in the direction of the object’s motion. Aeration should induce fluidization to reduce the strength of the

surrounding medium. Hypothesis 3: An asymmetric tip-based flow of air will control lift in granular media, reducing it by an amount proportional to the downward component of the airflow. Downward aeration should reduce the strength of the granular media below an object, thereby reducing the yield stress gradient that causes lift. Note that this is the opposite effect of what would occur in a gas or liquid, where the reaction force of a downward fluid jet would cause lift.

Here, we present (i) the results of experimental testing of our above hypotheses; (ii) the design, informed by these results, of a soft, steerable, burrowing robot with tip extension and directional fluidization and aeration; and (iii) the characterization and demonstration of the robot (Movie 1). The robot (Fig. 1 and fig. S1) builds upon our preliminary work on a vertical-burrowing device (36) to achieve the much more challenging tasks of controlled horizontal motion and steering. The robot realizes tip extension with a thin-walled tubular body of inelastic airtight fabric, inverted back inside itself. When pressurized, the tube everts, passing new material out of the tip to extend (Fig. 1C, left). Local, directional airflow at the tip of the robot is achieved by passing air through the core of the robot and out of the tip (Fig. 1C, center). Two nozzles at the robot's tip provide separate air supplies, one in line with the robot body for drag reduction and the other perpendicular to it for asymmetric flow and lift reduction (Fig. 1C, right). The robot is steered by tendons along the outside of its body that, when shortened, turn the tip of the robot. Although various other designs have been proposed for burrowing robots (56–59), few have demonstrated subterranean steering capabilities. Those that have demonstrated steering (33, 55) have only done so in glass or plastic beads at speeds over an order of magnitude slower than our device. The most well-known subterranean steering technology remains directional drilling (60); however, it requires heavy machinery and cannot create sharp turns. This robot provides a next step toward a practical burrowing robot—a tool for a wide range of shallow burrowing applications in sandy environments, noninvasive irrigation installation, pipe inspection, and extraterrestrial anchoring and soil sampling.

RESULTS

This section includes experimental testing of our three hypotheses, the design of the robot based on our experimental findings, and tests to characterize the performance and capabilities of the burrowing robot.



Movie 1. Overview of robotic burrowing with tip extension and granular fluidization. This video summarizes how tip extension, air fluidization, and asymmetry were used to create a soft burrowing robot.

Experimental testing

Tip extension reduces overall drag by an amount equal to skin drag

To test Hypothesis 1, which tip extension reduces drag force compared with intrusion by an amount equal to the skin drag, we compared the drag force exerted on a tip-extending robot with that on a rigid intruder in loose, dry sand (polydisperse silica particles 300–850 μm in diameter; see Materials and Methods). The results (Fig. 2) show that drag force during tip extension remained nearly constant, whereas during intrusion, it increased approximately linearly with length. Further, extrapolation of the two datasets suggests that they intersect near zero length. Together, these data suggest that, in support of the hypothesis, both the extending robot and rigid intruder experience the same frontal drag (~ 25 N), and the higher total drag on the intruder is indeed equal to the length-dependent skin drag.

Local granular fluidization reduces drag with nonlinear dependence on depth and airflow angle

Hypothesis 2 predicts that local aeration and granular fluidization reduces drag by an amount proportional to the component of the airflow in the direction of motion. To test this hypothesis, we conducted experiments in both the vertical and horizontal directions of motion with tip-localized airflow and found that the relationships between flow rate and drag were more complicated than predicted. In the first test, we measured the drag force on an intruder plunged vertically into a bed of loose, dry sand while we varied airflow rates (see Materials and Methods). As shown in Fig. 3, without airflow, force increases approximately linearly with depth; however, for higher flow rates, the relationship is nonlinear, with the force reduction becoming less substantial after a critical depth. This critical depth increases approximately linearly with flow rates above 21 liters/min, whereas power (fluidization air pressure times flow rate) increases exponentially (fig. S2). Although the force reduction was hypothesized, we did not expect this nonlinear behavior.

In the second test, we measured the resistive force on a horizontally oriented cylindrical intruder dragged horizontally through the sand. We varied both tip-localized airflow rate and angle from in line to perpendicular to the direction of movement (see Materials and Methods). The measured drag forces at a depth of 43 and 80 mm

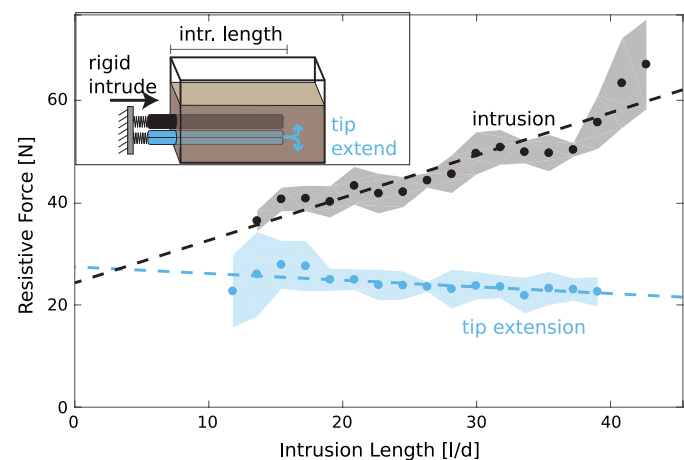


Fig. 2. Tip extension reduces resistive force by an amount equal to skin drag. Plot of the measured force required to advance both a rigid intruder (black) and a tip-extending robot (blue) horizontally in loose, dry sand. Linear fit lines (dashed) intersect at 26.8 N. Diameter = 22 mm, $N = 4$ trials; shaded error bars represent ± 1 SD.

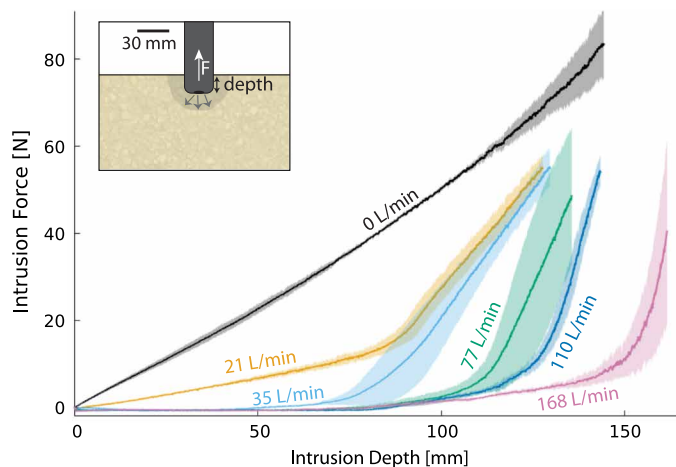


Fig. 3. Tip-based airflow reduces resistive force in vertical penetration in sand with a nonlinear dependence on depth. Resistive force versus depth for various tip flow rates plotted. Tip flow decreases resistive force to near zero until a critical depth beyond which it is less effective. $N = 3$ trials; shaded error bars represent ± 1 SD.

are shown in Fig. 4 (B and C), respectively. The data show that drag decreased roughly proportionally with increasing flow rates, as expected by our hypothesis. However, in contrast to our hypothesis, the drag reduction was not proportional to the component of airflow in the direction of motion: Perpendicular airflow also resulted in substantial drag reduction. Thus, our data show that nonaligned flows are less effective than aligned flows, but the magnitude of reduction is not as simple as a proportional term equal to the vector component of the airflow in the movement direction.

Asymmetric tip-based airflow reduces lift with nonmonotonic dependence on flow angle

We next tested our third and final hypothesis that asymmetric, directed airflow reduces lift by an amount proportional to the vertical component of the flow. Using the same setup as in the previous experiment, we measured lift forces on the intruder because it was dragged horizontally at two depths through a bed of loose, dry sand with various airflow rates and angles. Tests at depths of 43 and 80 mm are presented in Fig. 4 (D and E), respectively. At a depth of 43 mm without airflow, the symmetric intruder experienced a roughly constant positive lift of 1.4 ± 0.2 N in all tests. Increasing the flow rate decreased lift at most airflow angles. However, in contrast to our hypothesis, the airflow angle exhibited a nonmonotonic influence on lift. For shallow airflow angles between 0° and 30° , an increase in airflow angle meant an increase in lift to a maximum at 30° for all flow rates. Yet, as the angle increased from 30° to 60° , lift decreased to a minimum of nearly zero at the maximum flow rate, which remained roughly constant for angles between 60° and 90° . The results at a depth of 80 mm show a similar trend, with lower angles being less effective and higher angles being more effective at lift reduction. The local maximum is less pronounced, however. Although the lift reduction at high angles and flow rates was predicted by our hypothesis, the nonmonotonic behavior and local maximum at 30° were unexpected.

Robot design

On the basis of the experimental findings of the previous section, we designed a soft burrowing robot that uses tip extension to eliminate skin drag, tip-based flow to reduce form drag, and directional

tip flow combined with an asymmetric tip shape to control lift. This combination of tip extension and tip-based flow enables the robot to steer in curved shapes in dry sand (similar to that found in beach or desert dunes). First, we describe the design of the tip-extending robot body, then of the tip-based flow device, and lastly of the tendon steering mechanism, as shown in Fig. 1D and fig. S1.

Tip-extending body

Our tip-extending robot body is based on the principle that an inverted thin-walled tube everts when pressurized, as we previously demonstrated for above-ground vine-like robots (61). Because the interaction forces and internal pressures are higher than in these previous everting robots, there are more stringent requirements on the mechanical properties of the “skin” material. The skin must be circumferentially strong to resist the high hoop stress from internal pressure, torsionally stiff to resist twisting while turning, yet flexible to allow eversion. Our solution to this set of requirements is a custom bilayer composite airtight fabric, comprising a first layer with threads oriented axially and circumferentially and a second layer with threads oriented at 45° to these for torsional stiffness (see Materials and Methods).

We choose an intermediate scale for the diameter of the body (roughly 6 cm) based on trade-offs in scaling effects that make small and large diameters less desirable. In the first scaling effect, the maximum internal pressure of a robot decreases linearly with increasing diameter because of the linearly increasing hoop stress. Second, the pressure required to overcome the internal resistance during eversion decreases quadratically with increasing diameter (62). Last, both the force and the robot can apply to the medium at its tip and form drag scale proportionally with cross-sectional area balancing each other, regardless of diameter. With these three scaling trends in hand, there is an intermediate diameter where the difference between the maximum internal pressure and the pressure to overcome internal resistance is largest.

Tip-based flow device

To add airflow to the tip-extending body, we designed a tip-based flow device. To vary the tip flow direction, we use a two-nozzle system, each with its own air supply line; one nozzle is in line with the long axis of the body, whereas the other is oriented at 90° from this axis. Varying the flow between the two nozzles allows an approximate control over the flow direction. The two-channel air supply line runs through the core of the inverted body and is pushed forward as the robot grows.

The results of testing Hypothesis 3 show that tip-based airflow can reduce lift to nearly zero, but it is inconclusive whether it can produce negative lift, so we added a small asymmetric wedge at the tip that generates negative lift. The wedge projects out in front of the tip of the robot, so that its effects are not negated by localized aeration or fluidization. The combination of airflow and a wedge is synergistic. Airflow alone cannot cause the robot to dive, and a wedge alone would need to be very large to mitigate the full lift force, thus creating high drag. However, in combination, aeration can reduce drag and mostly eliminate lift, meaning only a small wedge (low drag) is required to have net negative lift. By modulating the amount of airflow in such a setup, we can control the lift experienced by the moving robot.

Steering

We steer the robot with pull tendons that run the length of the body, which each applies a moment to the entire body but only turns the tip of the robot. Tip extension allows only the tip of the

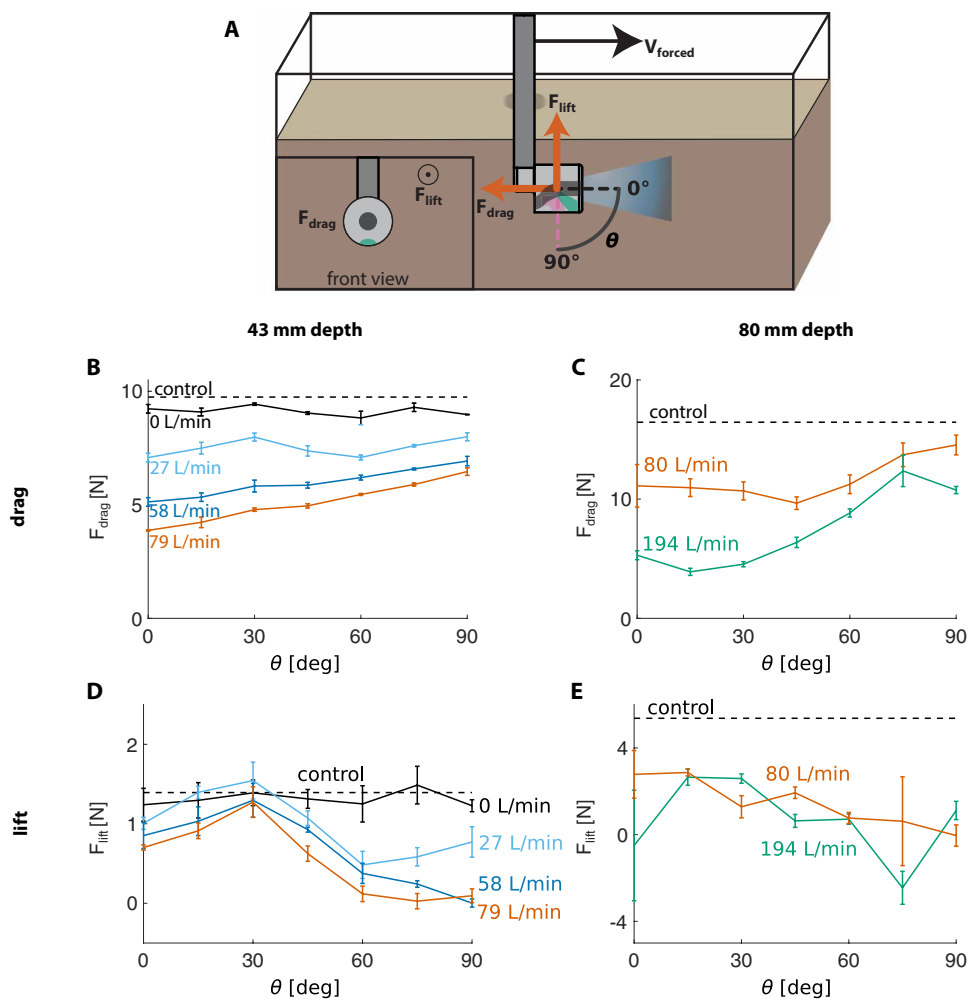


Fig. 4. Asymmetric tip-based airflow reduces drag and lift in horizontal intrusion with a nonmonotonic dependence on flow angle. (A) Experimental setup. Intruder was dragged horizontally at two depths, with varying tip flow angles. $N = 4$ trials for tests at 43-mm depth. $N = 1$ trial for tests at 80-mm depth with average and SD of steady-state forces plotted (see raw data in fig. S9). Error bars represent ± 1 SD. (B) Drag forces as a function of flow angle at a depth of 43 mm. (C) Drag forces as a function of flow angle at a depth of 80 mm. (D) Lift forces as a function of flow angle at a depth of 43 mm. (E) Lift forces as a function of flow angle at a depth of 80 mm.

robot to move with respect to the sand while the body is locked in place by the stationary sand. This tip-localized steering allows non-constant curvature shapes to be created with pull-tendons that run the length of the body. Although three tendons would allow three-dimensional motion, four tendons are used to allow simplified control with left-right and up-down steering. In this work, we use visual feedback to locate the robot via a mast that protrudes from the sand. However, localization of the buried robot tip could be achieved by existing methods including magnetic tracking (63, 64), inertial measurement units coupled with length sensing (65), or optical fiber sensing (66).

Whereas simply pulling the “left” or “right” tendon is sufficient for steering in the horizontal plane, moving outside of this plane is more complicated due to the effects of lift and aeration or fluidization. To transition from horizontal burrowing to vertical diving, the robot requires negative lift. Simply pulling the “down” tendon is

ineffective, because instead of the tip moving down, the proximal part of the body lifts up into the lower strength sand above it. We therefore require an additional downward airflow to dive. Transitioning from horizontal burrowing to vertical rising is easier and can be done either by pulling the “up” tendon or by reducing downward airflow. Turning from vertical diving to horizontal burrowing is also relatively easy because lift can again be used. The final transition from vertical rising to horizontal burrowing is not tested in this work but could be achieved with directed airflow and tendon steering.

Burrowing robot characterization and performance

We conducted a series of tests to characterize the effects of tip extension on anchoring, tip flow on drag, growth rate on drag, and tip flow on lift. We also conducted demonstrations of robot performance.

Tip extension and anchoring

Tip extension by eversion is reversible and allows the robot to retract by inverting its body without the concern of buckling, as can occur in air (67), because the surrounding sand supports the body. Inverting eliminates skin drag during removal from the ground and offers a method to control anchoring force. We measured the force required to pull a robot body out of the sand from the base and compared it with the force required to reinvert the robot (Fig. 5A); during reinversion, the force is much smaller and nearly constant with length.

Next, we explored how tip extension enables self-anchoring. Self-anchoring occurs when the tip reaction force that rejects the robot from the sand is less than the skin friction that holds the robot in place. The reaction force is roughly constant at a given depth, whereas skin friction increases with robot length. Thus, at a critical length, the reaction and friction forces balance each other. To test self-anchoring, we measured the reaction force on the base of the horizontally growing robot as a function of length, showing that after a critical length, the force drops to zero and self-anchoring occurs (Fig. 5B).

Effect of tip flow on drag

According to our results for a small, rigid test device in Fig. 4 (B and C), we expect the soft robot to require less pressure to grow as tip flow rate is increased (for a given angle of flow). To test this, we recorded the pressure required to start growing the robot as a function of tip flow rates. The results in Fig. 6A show that with increasing airflow, the pressure required to extend the robot decreases.

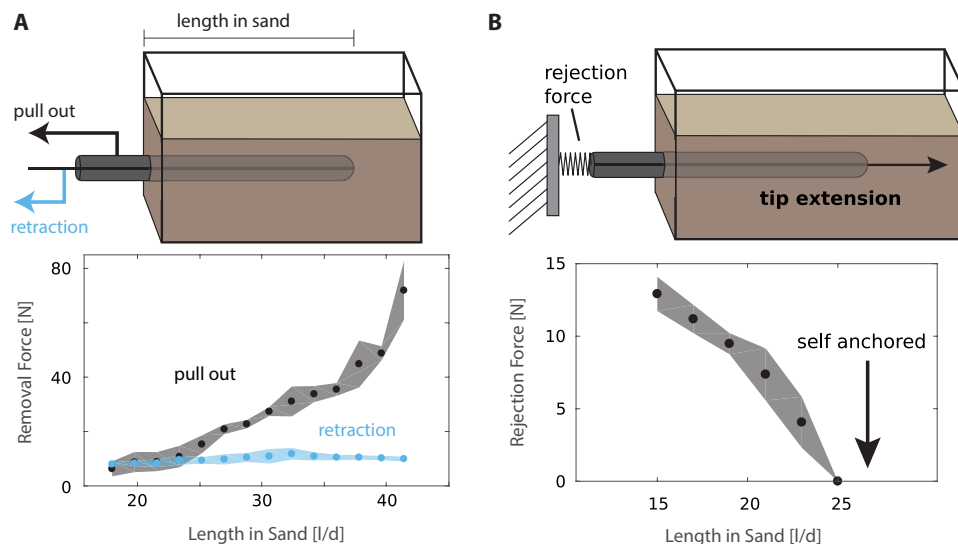


Fig. 5. Tip extension enables the robot to anchor in loose, dry sand. (A) Plot of measured force to remove a buried robot from sand by pulling out its body (black) and retracting it by reinversion (blue). Diameter = 22 mm, $N = 3$ trials; error bars represent ± 1 SD. (B) Plot of rejection force as a robot extends into sand as a function of length. As the robot extends more than 25 diameters in length, the reaction force is reduced to zero and the robot is self-anchored. Diameter = 22 mm, $N = 3$ trials; error bars represent ± 1 SD.

Effect of growth rate on drag

On the basis of tests with rigid intruders, drag in granular media is rate independent at slow speeds (68, 69) but increases roughly quadratically at high speeds as inertial forces become nonnegligible (11). We first performed low-speed vertical burrowing tests with a tip-extending robot body without aeration, controlling growth rate and measuring reaction force at the base (see Materials and Methods). The results (fig. S3) show that resistive force does not vary substantially at low speed in 1-mm-diameter poppy seeds (used because the robot cannot vertically penetrate sand without fluidization). Next, we performed a high-speed horizontal burrowing test in sand with speeds up to 480 cm/s, measuring reaction force and velocity. At these higher rates, the robot showed a relatively large (six times) change in reaction force for an increase in speed of only two times (Fig. 6B). Images of one of the tests are shown in Fig. 6C, showing the robot covering 30 cm in 0.08 s.

Effect of tip flow on lift

On the basis of the results shown in Fig. 4 (D and E), we expect a horizontally burrowing robot to demonstrate different growth paths as the downward airflow rate is varied. We recorded the position of a vertical mast attached to the tip of the robot and protruding out of the sand as the robot grew horizontally with various aerating flow rates. Figure 6D shows that at low flow rates, lift causes the robot to travel at an angle substantially above horizontal; at intermediate flow rates, lift can be balanced near or below zero to enable diving; and at high flow rates, surfacing once again occurs, likely due to the reaction force of the airflow jet. The images in Fig. 6 (E and F) show the cases of low and high tip flow, respectively.

Robot performance

The subterranean performance of the burrowing robot in the horizontal plane was demonstrated by traversing a sand bed in straight, curved, and serpentine paths (Fig. 7). In the first demonstration, the robot successfully traversed 60 cm of sand at a depth of about 8 cm with a constant downward flow rate of 140 liters/min and a speed of

2 cm/s. In the second demonstration, the robot made a right turn under the same conditions by increasing tension on the right-side tendon. In the third demonstration, the robot turned right and then left to avoid a buried obstacle using tendon steering. The robot remained buried at a relatively constant depth, demonstrating depth control and horizontal planar steering.

The robot's performance in vertical burrowing was demonstrated with straight and "U"-shaped paths. In the first demonstration, the robot burrowed to a depth of 35 cm at 2 cm/s. Next, it used tendons and a controlled aeration angle to burrow down, underneath, and then up to the far side of a buried obstacle. These demonstrations show the robot's ability to navigate vertical and horizontal obstacles while maintaining depth control.

The tension in the steering tendon is largely independent of the surrounding medium for a given radius of curvature.

Under a constant tendon displacement,

body pressure, and radius of curvature, the tendon tension increased slightly with length as it grew in a bend with a 46-cm radius. As shown in fig. S4, the tension was roughly equivalent when turning in air, in loose, dry sand without airflow, and in sand with local airflow.

DISCUSSION

Here, we tested three hypotheses related to controlling subterranean interaction forces in granular media. We used the results of these tests to design a fast, steerable, burrowing soft robot; characterized the behavior of the robot; and demonstrated its capabilities. In this section, we discuss the implications of our experimental findings and robot performance.

As shown in Hypothesis 1 testing, tip extension reduces overall drag by an amount equal to the skin drag, meaning that with only frontal drag remaining, the force-resisting motion of the tip of our tip-extending robot is independent of length and path at a fixed depth. This is especially important as robot length increases; without tip extension, the force-resisting motion would continue to rise and, eventually, the robot could no longer move forward. Furthermore, for curved paths in robots without tip extension, we expect that the body would experience even higher drag due to capstan friction, which increases exponentially with total path curvature (70).

Tip extension also decouples the magnitude of the external force required to move the body of the robot (e.g., pull it from the ground) and the magnitude of force required to move the tip (e.g., grow or retract). This means that the robot can modulate its anchoring force by roughly seven times at a length of 90 cm (Fig. 5A) and by more for longer bodies, allowing it to control whether it remains firmly planted in the ground or slips easily out. Branching is also possible with this morphology of robot (71), potentially enabling multibranching root-like structures to further increase these anchoring forces (72).

At the same time, the decoupling of anchoring and growth forces results in a phenomenon we refer to as self-anchoring, wherein the

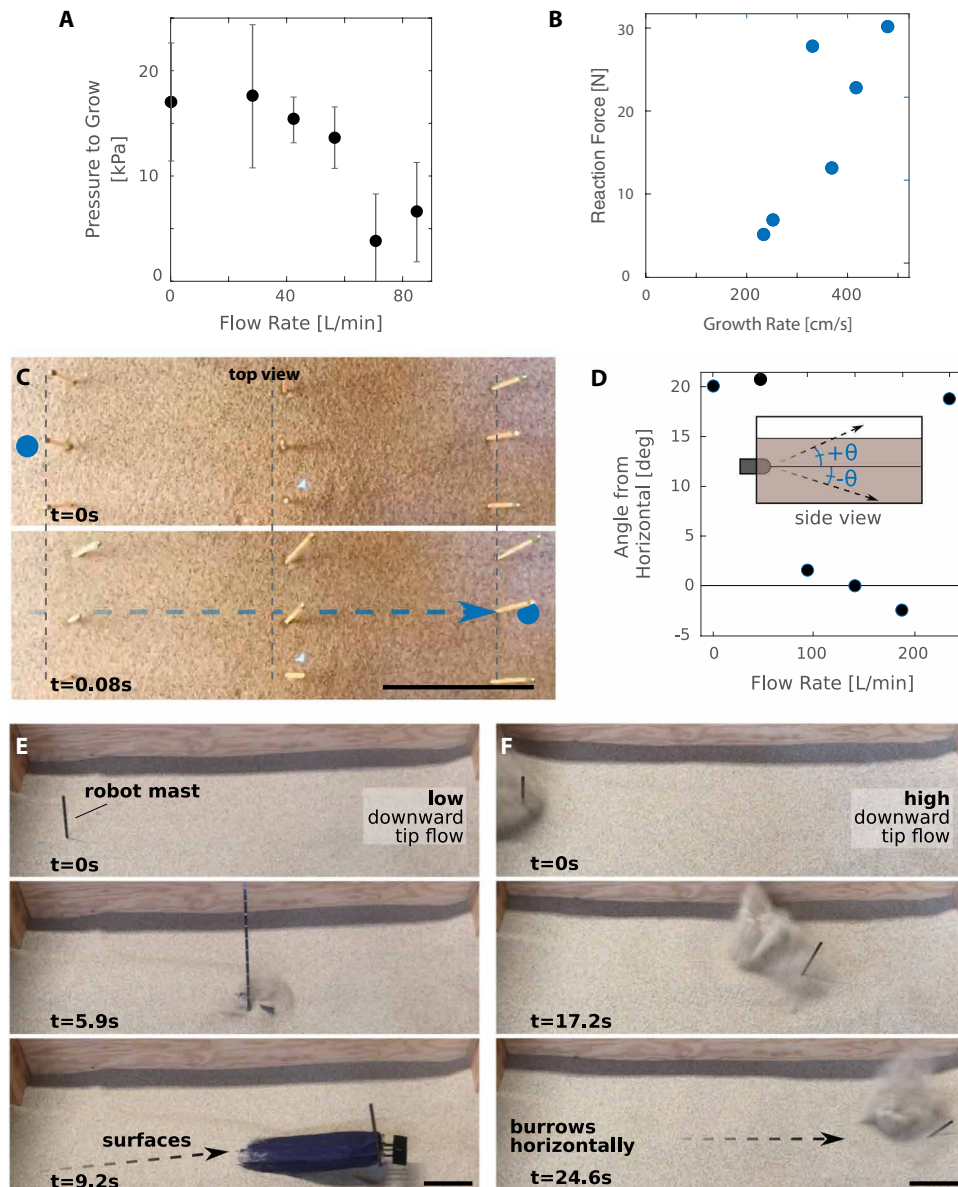


Fig. 6. Characterization of the effects of tip flow and growth rate on burrowing. (A) Plot of internal pressure of full-sized robot (see Materials and Methods) required to grow through sand as a function of tip airflow rate. The pressure to grow in the absence of sand has been zeroed out. $N = 5$ trials; error bars represent one SD. (B) Plot of reaction force as a function of horizontal tip extension rate in sand. $N = 1$ trial. (C) Overhead images of high-speed horizontal burrowing. A blue dot marks the tip of the robot, and vertical matchsticks help visualize its passage underneath. Vertical dashed lines mark the initial position of the tips of the matchsticks, which are disturbed (bottom image) after the robot passes beneath (see movie S5). (D) Effect of airflow rate on horizontal burrowing trajectory angle. $N = 1$ trial. (E) Effect of tip airflow on path of growth. Low downward airflow rates do not reduce lift sufficiently, and the robot surfaces. (F) However, with the increased downward flow, lift is reduced, and the robot is able to burrow horizontally (see movie S5). Scale bars denote 10 cm.

friction along the length of the robot body becomes larger than the reaction force at the tip beyond a certain length (Fig. 5B and fig. S8). Although tested in horizontal burrowing in this work, the effect should occur for vertical burrowing as well. The minimum length at which the robot will self-anchor can be approximated as $r/2\mu$ in horizontal burrowing and r/μ in vertical burrowing, where r is robot radius and μ is the coefficient of friction between the robot and the

environment (see the Supplementary Materials for derivation). Self-anchoring is especially important for cases where it is difficult to provide enough reaction force to prevent rejection from the soil. For instance, when burrowing in extra-terrestrial settings with low gravity, self-anchoring is beneficial because it reduces the mass and cost of the robot base needed. Critically, self-anchoring allows a robot to apply forces on the environment that exceed its own weight.

Another advantage of steering with tip extension is the ability to create curved paths during subterranean navigation. A long continuum body without tip extension that is pushed through the soil is constrained to follow a path of constant curvature, because the whole body must move forward (73). However, with tip extension and tip-localized steering, the robot is free to change curvature throughout its path because the more proximal body remains stationary while the tip can extend in a range of directions. Our steerable robot is also hollow, meaning that it can create hollow conduits for applications such as installing wire or irrigation lines. Such conduits could be placed without digging a trench and curve around and under obstacles as needed.

Last, our method of pneumatic tip extension enables the soft robot to burrow at high speeds. The speed (480 cm/s) achieved by the subsurface movement of the simple robot in Fig. 6 is near its limit in air. Higher speeds require more internal pressure, which is limited by the hoop stress of the fabric body. The full-sized robot with tip flow and steering was operated at 2 cm/s. For comparison, previous steerable burrowing robots burrowed at 0.11 cm/s in glass beads (55), previous root-like robots that grew by additive manufacturing burrowed at 0.0067 cm/s in plastic beads (33), and the InSight HP³ probe burrowed at 0.14 cm/s (22) in sand on Earth. None of these designs incorporated a mechanism like aeration to reduce the strength of the surrounding medium. In living examples, moles (74)

and razor clams (75) can burrow up to 1 cm/s, and the sandfish lizard (53) can burrow up to 10 cm/s in short bursts.

As shown in the results of Hypothesis 2 testing, aeration reduces drag in granular media, and although the relationship among depth, flow angle, and force is nonlinear, our characterization results show that tip flow is an effective method for reducing the force required to burrow in our robot. The first interesting nonlinearity we found

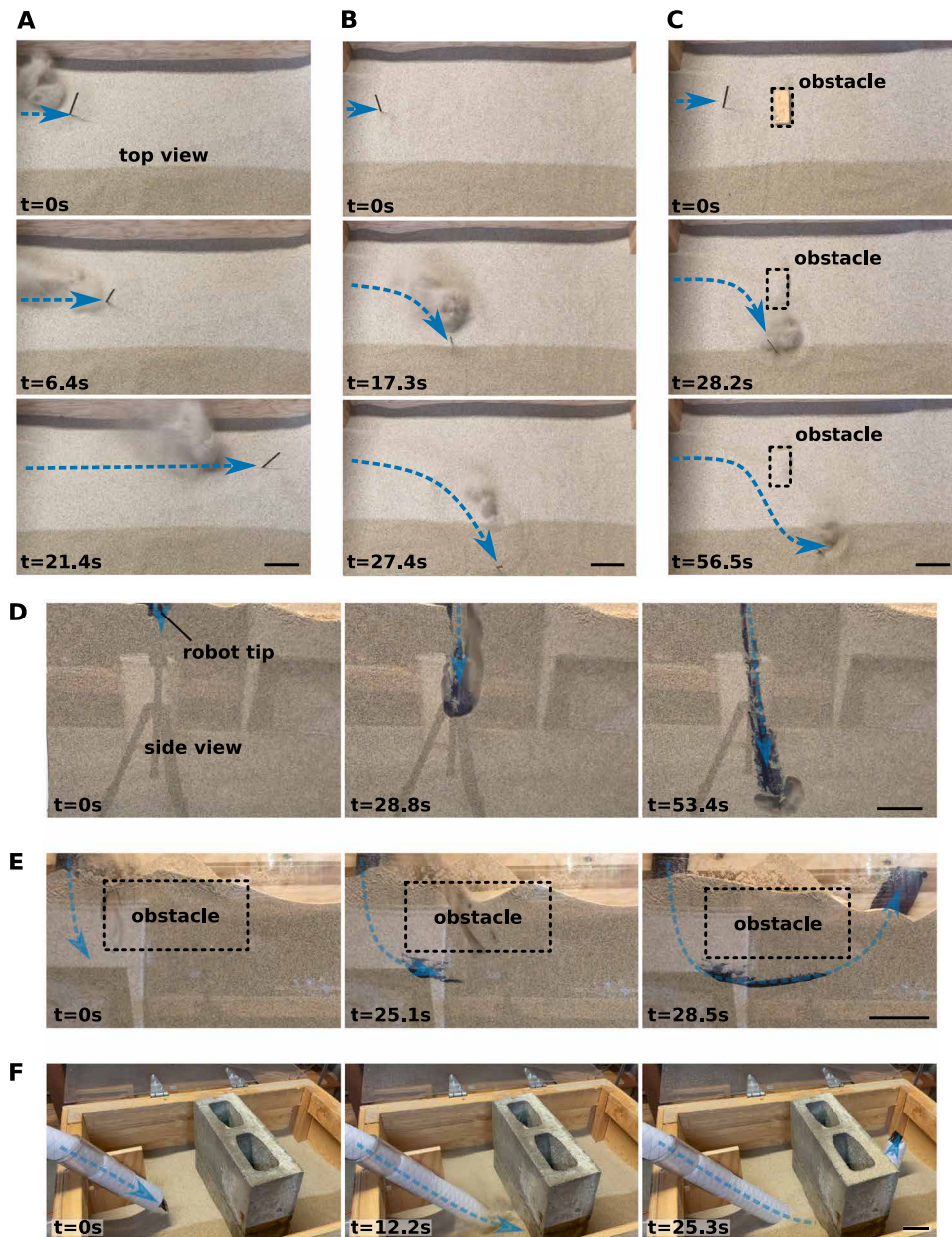


Fig. 7. Robot steering demonstrations. (A) Controlled horizontal burrowing to 60-cm length at a depth of 8 cm. (B) Right turn at a depth of 8 cm. (C) Right and then left turn to navigate around an obstacle. (D) Vertical burrowing up to 35 cm deep. (E) Navigating down, under, and up on the other side of a buried obstacle. (F) Navigating down, under, and up on the other side of a cinder block wall. Arrows follow the robot's path and point to the tip of the robot. See movies S3, S4, and S6. Scale bars denote 10 cm.

is in the relationship between drag and depth in vertical burrowing while aerating. For a given flow rate, force is reduced to near zero until a critical depth, beyond which the effectiveness of aeration decreases, but is still present (Fig. 3). Texier *et al.* (76) also observed a qualitatively similar behavior in an experiment that used a vibrating vertical intruder to fluidize a granular media. A possible explanation is that the lithostatic pressure and drag force increase with depth (9) to a point where the air can no longer mobilize the grains and fluidization is suppressed. Furthermore, with increasing depth, it likely becomes more difficult to fluidize the volume of sand above

the aeration source. Because parameters are varied to increase the critical depth, the slope of the drag versus depth curve in the region beyond the critical depth increases. This could be caused by a higher lithostatic pressure or increased sand compactness due to the high-pressure airflow itself.

The second nonlinearity that we found is in the relationship between flow direction and drag in horizontal burrowing. Although tip flow in line with the direction of movement is most effective at reducing drag, we also found that airflow perpendicular to the movement was still effective, although none of the component of flow was in the direction of movement (Fig. 4, B and C). One possible explanation is that air directed perpendicular to the motion (here, downward flow for a horizontal motion) also fluidized the sand in front of the robot, as suggested by the visualization of particle flow in figure 6 in (36) showing the movement of particles above and around the air source. This might also explain why the force reduction in vertical burrowing is much greater than in horizontal burrowing for a given flow rate: If the fluidized region tends to spread upward from the source, then it would be less effective at reducing drag around the tip of the robot when moving horizontally.

It is important to mention that the method of aeration and air fluidization used in our robot was only demonstrated in loose, dry, noncohesive sand. The effects observed should translate to other dry granular media of a similar particle size and shape, such as other sands and extraterrestrial regolith, and to media with larger and more spherical particles, but with higher required flow rates (4, 77). The effectiveness of aeration is likely limited in cohesive, damp, or saturated earth environments. However, water could be used for the fluidizing flow in these soils, as used by the southern sand octopus

(*O. kaurna*) (42). Similarly, vibration-induced liquefaction, such as in sonic drilling (51, 78), or an auger drill (79) could be implemented in the tip-based device on our robot.

Our method of aeration uses energy from a compressed gas to reduce the reaction force required to burrow. For a critical depth of 15 cm, a flow rate of 168 liters/min at 130 kPa was used, with a corresponding power of 550 W. Intruding at 1 cm/s for 15 s required 42 liters of air and 8.3 kJ of energy but less than 10 N of force. For comparison, the work done by the intruder without aeration was only 5.8 J but required more than 80 N of force. This suggests that

eration does not save energy in burrowing but reduces force by an order of magnitude, allowing the robot to be soft and, therefore, steerable. The reduced reaction force would be useful in low-gravity applications, such as planetary or asteroid exploration, where reaction forces are difficult to produce. Projects such as NASA's OSIRIS-REx's asteroid sample return mission already carry compressed gas for granular fluidization (80).

As shown in the results of Hypothesis 3 testing, asymmetric, downward-directed airflow can control lift, although the relationship between flow angle and lift reduction is nonmonotonic. The result is unique to granular media, because in a fluid, such downward airflow would increase, rather than reduce, lift. Increasing the component of the downward airflow by varying the flow direction from horizontal to vertical does not monotonically decrease lift. Instead, around 30° from horizontal, there is a region of angles that actually increases lift (Fig. 4, D and E). At deeper depths and higher flow rates, this maximum is less pronounced. This increase does not appear without airflow, suggesting that it is not a product of nozzle geometry but could be an effect of airflow position and orientation. Although more study is needed to understand the granular physics of this behavior, we do note that the angle of repose of dry sand is about 30° (81). Ding *et al.* (10) found that lift in granular media was caused by sand being pushed up a slip plane, suggesting that aeration or fluidization along a slip direction could affect lift differently than at other angles. Last, we note that although lift increases with depth, it eventually saturates (9), suggesting that lift would still be an issue for a robot that burrows horizontally much deeper than ours, but would be smaller in comparison with the ever-increasing drag force.

Our work presents a terradynamic understanding of burrowing in granular media and applies the key results to design a soft robot that controls subterranean interaction forces to achieve fast, steerable burrowing in three dimensions. Although our method of burrowing may not be ideal for soil penetration beyond a few meters, it offers improved performance in long, shallow, directional burrowing. Potential applications on Earth include soil sampling; minimally invasive irrigation, wire, or geothermal loop installation without trenches; erosion control; search and rescue; and granary inspection. Our method is also well suited for dry, low-gravity, extraterrestrial environments, where reactive forces may be difficult to produce. Example applications include thermal sensor placement on Mars, volcanic tunnel exploration on the moon, asteroid sampling or anchoring, and granular ice exploration on Enceladus, a moon of Saturn. More broadly, the mechanisms for controlling subterranean forces investigated in this paper are useful beyond the scope of a small burrowing robot. Future work could examine integrating tip extension with conventional drilling and exploration technologies.

MATERIALS AND METHODS

Robot fabrication

Details of the burrowing robot are shown in Fig. 1, fig. S1, and movies S1 and S2. It features three main components: the everting body, the tip-flow air supply line, and the steering mechanism.

The everting body is made of two layers of 50- μ m-thick silicone and urethane impregnated ripstop nylon (Seattle Fabrics; measured initial modulus of 74 MPa along fibers, 9.0 MPa at 45° bias), adhered together into a 60-mm-diameter, 2-m-long tube with room

temperature vulcanizing silicone adhesive (Sil-Poxy, Smooth-On Inc.). One layer is oriented with its threads along the axial and circumferential axis of the robot and the other at a 45° angle for axial and torsional stiffness, respectively. A string is attached to the tail of the robot that can be pulled to retract the robot. The end of the body is sealed around a solid, 60-mm-diameter Delrin cylinder fixed to an air supply, with dynamic seals for the tail string and tip-flow air supply line to pass through.

The air supply line is made of two nested concentric nylon tubes (inner diameters of 2.4 and 6.4 mm) for separate forward and perpendicular (downward) airflow, wrapped in a carbon fiber braid and polytetrafluoroethylene sleeve with an outer diameter of 9.5 mm for increased torsional stiffness and reduced friction, respectively. The forward-facing nozzle is a simple hole, whereas the downward nozzle is “T” shaped, spreading the flow to the width of the robot. Attached to the airflow nozzle is a 55 mm-by-25 mm fiberglass wedge, at a 10° angle of attack. It is positioned 15 mm in front of the downward nozzle so that the aeration does not negate its effects. The forward airflow supply line passes through the center of the wedge, negating its effects during vertical burrowing. Inside the body of the robot but around the airflow supply line is a constriction ring made of 6-mm-thick neoprene foam that seals the inverted body material to the supply lines at the tip. Sealing at the distal end of the inverted body material allows the internal body pressure to equalize on either side of the material, reducing the pressure and friction that it exerts on the supply line. This helps prevent the air supply line from being spit out of the body as it everts and reduces tension on the supply line while increasing tension in the body wall, enabling the body to take a stable shape.

Four 1.6-mm-diameter braided steel tendons control steering. They are equally spaced around the circumference of the body, running through 2.4-mm-inner diameter, 2-cm-long nylon guides adhered 2 cm apart along the length of the body with silicone adhesive, and covered in a ripstop nylon sheath. As the tendon is shortened, these nylon guides collide, setting a minimum radius of curvature of 19 cm that prevents kinking in any one section of the robot.

The robot weighs 780 g including the everting body, airflow supply line, and seals. It requires an additional 390 g of body and airflow tube per meter of length. The robot body pressure is supplied by up to 150 kPa of compressed air or nitrogen, whereas the forward and downward airflow tubes can supply up to 30 and 300 liters/min of compressed gas from a 1-MPa source, respectively.

Experimental methods

Two nearly identical dry, silica sands were used in this study. One was Cemex Lapis Lustre 30 Mesh Sand with polydisperse particles ranging in diameter from 300 to 850 μ m. The second was Quikrete Filter Sand with polydisperse particles ranging in diameter from 425 to 850 μ m. Sand beds were fluidized between all trials with air or nitrogen for a repeatable initial condition with an approximate volume fraction of 58%. Please see the “Experimental methods” section in the Supplementary Materials for a complete description of the experimental methods.

SUPPLEMENTARY MATERIALS

robotics.sciencemag.org/cgi/content/full/6/55/eabe2922/DC1

Experimental methods

Derivation of critical length for self-anchoring

Figs. S1 to S9

Movies S1 to S6

REFERENCES AND NOTES

- NASA, Mars curiosity rover, <https://mars.nasa.gov/msl/home/> [accessed 13 August 2020].
- World Health Organization Institute, Ships and technology used during the titanic expeditions, www.who.edu/know-your-ocean/ocean-topics/underwater-archaeology/rms-titanic/ships-technology-used-during-the-titanic-expeditions/ [accessed 13 August 2020].
- TEPCO, Application of robot technology, www.tepco.co.jp/en/decommission/principles/robot/index-e.html [accessed 13 August 2020].
- C. Li, T. Zhang, D. I. Goldman, A terradynamics of legged locomotion on granular media. *Science* **339**, 1408–1412 (2013).
- R. D. Maladen, Y. Ding, P. B. Umbanhowar, A. Kamor, D. I. Goldman, Mechanical models of sandfish locomotion reveal principles of high performance subsurface sand-swimming. *J. R. Soc. Interface* **8**, 1332–1345 (2011).
- J. Duran, *Sands, Powders, and Grains: An Introduction to the Physics of Granular Materials* (Springer Science & Business Media, 2012).
- T. Zhang, D. I. Goldman, The effectiveness of resistive force theory in granular locomotion. *Phys. Fluids* **26**, 101308 (2014).
- K. Wieghardt, Experiments in granular flow. *Annu. Rev. Fluid Mech.* **7**, 89–114 (1975).
- F. Guillard, Y. Forterre, O. Pouliquen, Lift forces in granular media. *Phys. Fluids* **26**, 043301 (2014).
- Y. Ding, N. Gravish, D. I. Goldman, Drag induced lift in granular media. *Phys. Rev. Lett.* **106**, 028001 (2011).
- F. Q. Potiguar, Y. Ding, Lift and drag in intruders moving through hydrostatic granular media at high speeds. *Phys. Rev. E* **88**, 012204 (2013).
- D. F. Youch, "Efficient calculation of earth penetrating projectile trajectories," thesis, Naval Postgraduate School, Monterey, CA (2006).
- R. D. Maladen, P. B. Umbanhowar, Y. Ding, A. Mase, D. I. Goldman, Granular lift forces predict vertical motion of a sand-swimming robot, in *Proceedings of the 2011 IEEE International Conference on Robotics and Automation (ICRA)* (IEEE, 2011), pp. 1398–1403.
- E. Shuter, W. E. Teasdale, *Application of Drilling, Coring, and Sampling Techniques to Test Holes and Wells* (Department of the Interior, U.S. Geological Survey, 1989), vol. 2.
- G. Girmscheid, C. Schexnayder, Tunnel boring machines. *Pract. Period. Struct. Design Construct.* **8**, 150–163 (2003).
- A. T. Bourgoyne Jr, K. K. Millheim, M. E. Chenevert, F. S. Young Jr, *Applied Drilling Engineering* (Society of Petroleum Engineers, 1986), vol. 2.
- E. N. Allouche, S. T. Ariaratnam, J. S. Lueke, Horizontal directional drilling: Profile of an emerging industry. *J. Construct. Eng. Manag.* **126**, 68–76 (2000).
- K. Nagaoka, T. Kubota, M. Otsuki, S. Tanaka, Experimental study on autonomous burrowing screw robot for subsurface exploration on the moon, in *Proceedings of the 2008 IEEE/RSJ International Conference on Intelligent Robots and Systems (IROS)* (IEEE, 2008), pp. 4104–4109.
- C. Pitcher, Y. Gao, Analysis of drill head designs for dual-reciprocating drilling technique in planetary regoliths. *Adv. Space Res.* **56**, 1765–1776 (2015).
- Y. Gao, A. Ellery, M. Jaddou, J. Vincent, S. Eckersley, Planetary micro-penetrator concept study with biomimetic drill and sampler design. *IEEE Trans. Aerospace Electron. Syst.* **43**, 875–885 (2007).
- J. Grygorczuk, Ł. Wiśniewski, B. Kędziora, M. Borys, R. Przybyła, T. Kuciński, M. Ossowski, W. Konior, O. Krömer, T. Spohn, J. Tokarz, M. Białek, Hammering mechanism for hp3 experiment (insight), in *Proceedings of the 43rd Aerospace Mechanisms Symposium* (NASA Ames Research Center, 4 to 6 May 2016), pp. 415–428.
- T. Wippermann, T. L. Hudson, T. Spohn, L. Witte, M. Scharringhausen, G. Tsakyridis, M. Fittock, O. Krömer, S. Hense, M. Grott, J. Knollenberg, R. Lichtenheldt, Penetration and performance testing of the HP³ mole for the insight mars mission. *Planet. Space Sci.* **181**, 104780 (2020).
- NASA, Nasa insight's 'mole' ends its journey on mars, <https://mars.nasa.gov/news/8836/nasa-insights-mole-ends-its-journey-on-mars/?site=insight> [accessed 18 May 2021].
- A. Dexter, Mechanics of root growth. *Plant Soil* **98**, 303–312 (1987).
- A. G. Bengough, C. E. Mullins, Mechanical impedance to root growth: A review of experimental techniques and root growth responses. *J. Soil Sci.* **41**, 341–358 (1990).
- L. Clark, W. Whalley, P. Barraclough, How do roots penetrate strong soil? in *Roots: The Dynamic Interface Between Plants and the Earth*, J. Abe, Ed. (Springer, 2003), pp. 93–104.
- A. Bengough, B. McKenzie, Sloughing of root cap cells decreases the frictional resistance to maize (*Zea mays* L.) root growth. *J. Exp. Bot.* **48**, 885–893 (1997).
- M. Iijima, Y. Kono, Development of golgi apparatus in the root cap cells of maize (*Zea mays* L.) as affected by compacted soil. *Ann. Bot.* **70**, 207–212 (1992).
- M. Iijima, T. Higuchi, P. W. Barlow, A. G. Bengough, Root cap removal increases root penetration resistance in maize (*Zea mays* L.). *J. Exp. Bot.* **54**, 2105–2109 (2003).
- C. Glenday, *Guinness World Records 2008* (Bantam, 2008).
- J. A. Kemperman, B. V. Barnes, Clone size in american aspens. *Can. J. Bot.* **54**, 2603–2607 (1976).
- A. Sadeghi, A. Tonazzini, L. Popova, B. Mazzolai, A novel growing device inspired by plant root soil penetration behaviors. *PLOS ONE* **9**, e90139 (2014).
- A. Sadeghi, A. Mondini, B. Mazzolai, Toward self-growing soft robots inspired by plant roots and based on additive manufacturing technologies. *Soft Robot.* **4**, 211–223 (2017).
- A. Sadeghi, E. Del Dottore, A. Mondini, B. Mazzolai, Passive morphological adaptation for obstacle avoidance in a self-growing robot produced by additive manufacturing. *Soft Robot.* **7**, 85–94 (2020).
- A. Sadeghi, A. Tonazzini, L. Popova, B. Mazzolai, Robotic mechanism for soil penetration inspired by plant root, in *Proceedings of the 2013 IEEE International Conference on Robotics and Automation (ICRA)* (IEEE, 2013), pp. 3457–3462.
- N. D. Naclerio, C. M. Hubicki, Y. O. Aydin, D. I. Goldman, E. W. Hawkes, Soft robotic burrowing device with tip-extension and granular fluidization, in *Proceedings of the 2018 IEEE/RSJ International Conference on Intelligent Robots and Systems (IROS)* (IEEE, 2018), pp. 5918–5923.
- Y. Ozkan-Aydin, M. Murray-Cooper, E. Aydin, E. N. McCaskey, N. Naclerio, E. W. Hawkes, D. I. Goldman, Nutation aids heterogeneous substrate exploration in a robophysical root, in *Proceedings of the 2019 2nd IEEE International Conference on Soft Robotics (RoboSoft)* (IEEE, 2019), pp. 172–177.
- K. M. Dorgan, The biomechanics of burrowing and boring. *J. Exp. Biol.* **218**, 176–183 (2015).
- O. Zik, J. Stavans, Y. Rabin, Mobility of a sphere in vibrated granular media. *Europhys. Lett.* **17**, 315–319 (1992).
- I. MacDonald, "Burial mechanics of the pacific sandfish: The role of the ventilatory pump and physical constraints on the behavior," thesis, Northern Arizona University (2015).
- E. Trueman, The mechanism of burrowing of the mole crab, *Emerita. J. Exp. Biol.* **53**, 701–710 (1970).
- J. Montana, J. K. Finn, M. D. Norman, Liquid sand burrowing and mucus utilisation as novel adaptations to a structurally-simple environment in octopus kaurma stranks, 1990. *Behaviour* **152**, 1871–1881 (2015).
- E. Trueman, The burrowing activities of bivalves. *Symp. Zool. Soc. Lond.* **22**, 167–186 (1968).
- A. G. Winter, R. L. Deits, A. E. Hosoi, Localized fluidization burrowing mechanics of *Ensis directus*. *J. Exp. Biol.* **215**, 2072–2080 (2012).
- A. G. Winter, R. L. H. Deits, D. S. Dorsch, A. H. Slocum, A. E. Hosoi, Razor clam to roboclam: Burrowing drag reduction mechanisms and their robotic adaptation. *Bioinspir. Biomim.* **9**, 036009 (2014).
- J. J. Tao, S. Huang, Y. Tang, Sbor: A minimalistic soft self-burrowing-out robot inspired by razor clams. *Bioinspir. Biomim.* **15**, 055003 (2020).
- K. Zacny, D. Currie, G. Paulsen, T. Szwarc, P. Chu, Development and testing of the pneumatic lunar drill for the emplacement of the corner cube reflector on the moon. *Planet. Space Sci.* **71**, 131–141 (2012).
- B. M. Das, *Principles of Foundation Engineering 6th Edition* (Thomson, 2007).
- A. G. Bodine, Sonic drilling device, U.S. Patent 3,684,037 (1972).
- J. C. Barrow, The resonant sonic drilling method: An innovative technology for environmental restoration programs. *Groundwater Monit. Rem.* **14**, 153–160 (1994).
- J. Barrow, Sonic drilling method and apparatus, U.S. Patent 5,562,169 (1996).
- E. N. Arnold, Identifying the effects of history on adaptation: Origins of different sand-diving techniques in lizards. *J. Zool.* **235**, 351–388 (1995).
- R. D. Maladen, Y. Ding, C. Li, D. I. Goldman, Undulatory swimming in sand: Subsurface locomotion of the sandfish lizard. *Science* **325**, 314–318 (2009).
- K. S. Norris, J. L. Kavanau, The burrowing of the western shovel-nosed snake, *Chionactis occipitalis* hallowell, and the undersand environment. *Copeia* **1966**, 650–664 (1966).
- M. Barenboim, A. Degani, Steerable burrowing robot: Design, modeling and experiments, in *Proceedings of the 2020 IEEE International Conference on Robotics and Automation (ICRA)* (IEEE, 2020), pp. 829–835.
- R. A. Russell, Crabot: A biomimetic burrowing robot designed for underground chemical source location. *Adv. Robot.* **25**, 119–134 (2011).
- B. Liu, Y. Ozkan-Aydin, D. I. Goldman, F. L. Hammond, Kirigami skin improves soft earthworm robot anchoring and locomotion under cohesive soil, in *Proceedings of the 2019 2nd IEEE International Conference on Soft Robotics (RoboSoft)* (IEEE, 2019), pp. 828–833.
- K. Isaka, K. Tsumura, T. Watanabe, W. Toyama, M. Sugawara, Y. Yamada, H. Yoshida, T. Nakamura, Development of underwater drilling robot based on earthworm locomotion. *IEEE Access* **7**, 103127–103141 (2019).
- D. Ortiz, N. Gravish, M. T. Tolley, Soft robot actuation strategies for locomotion in granular substrates. *IEEE Robot. Autom. Lett.* **4**, 2630–2636 (2019).
- X. Yan, S. T. Ariaratnam, S. Dong, C. Zeng, Horizontal directional drilling: State-of-the-art review of theory and applications. *Tunnell. Underground Space Technol.* **72**, 162–173 (2018).
- E. W. Hawkes, L. H. Blumenschein, J. D. Greer, A. M. Okamura, A soft robot that navigates its environment through growth. *Sci. Robot.* **2**, eaa3028 (2017).

62. L. H. Blumenschein, A. M. Okamura, E. W. Hawkes, Modeling of bioinspired apical extension in a soft robot, in *Conference on Biomimetic and Biohybrid Systems*, M. Mangan, M. Cutkosky, A. Mura, P. Verschure, T. Prescott, N. Lepora, Eds. (Springer, 2017), pp. 522–531.
63. C. Watson, T. K. Morimoto, Permanent magnet-based localization for growing robots in medical applications, in *Proceedings of the 2020 IEEE International Conference on Robotics and Automation (ICRA)* (IEEE, 2020).
64. B. Park, H. Myung, Underground localization using dual magnetic field sequence measurement and pose graph slam for directional drilling. *Measure. Sci. Technol.* **25**, 125101 (2014).
65. Z. Yanshun, W. Shuwei, F. Jiancheng, Measurement-while-drilling instrument based on predestined inertial measurement unit. *IEEE Trans. Instrument. Measur.* **61**, 3295–3302 (2012).
66. R. Xu, A. Yurkewich, R. V. Patel, Curvature, torsion, and force sensing in continuum robots using helically wrapped fbg sensors. *IEEE Robot. Autom. Lett.* **1**, 1052–1059 (2016).
67. M. M. Coad, R. P. Thomasson, L. H. Blumenschein, N. S. Usevitch, E. W. Hawkes, A. M. Okamura, Retraction of soft growing robots without buckling. *IEEE Robot. Autom. Lett.* **5**, 2115–2122 (2020).
68. R. Albert, M. Pfeifer, A.-L. Barabási, P. Schiffer, Slow drag in a granular medium. *Phys. Rev. Lett.* **82**, 205–208 (1999).
69. B. Percier, S. Manneville, J. N. McElwaine, S. W. Morris, N. Taberlet, Lift and drag forces on an inclined plow moving over a granular surface. *Phys. Rev. E* **84**, 051302 (2011).
70. J. H. Jung, N. Pan, T. J. Kang, Capstan equation including bending rigidity and non-linear frictional behavior. *Mech. Mach. Theory* **43**, 661–675 (2008).
71. L. H. Blumenschein, L. T. Gan, J. A. Fan, A. M. Okamura, E. W. Hawkes, A tip-extending soft robot enables reconfigurable and deployable antennas. *IEEE Robot. Autom. Lett.* **3**, 949–956 (2018).
72. S. B. Mickovski, A. G. Bengough, M. F. Bransby, M. C. R. Davies, P. D. Hallett, R. Sonnenberg, Material stiffness, branching pattern and soil matric potential affect the pullout resistance of model root systems. *Eur. J. Soil Sci.* **58**, 1471–1481 (2007).
73. R. J. Webster III, J. S. Kim, N. J. Cowan, G. S. Chirikjian, A. M. Okamura, Nonholonomic modeling of needle steering. *Int. J. Robot. Res.* **25**, 509–525 (2006).
74. R. Seymour, P. Withers, W. Weathers, Energetics of burrowing, running, and free-living in the namib desert golden mole (*Eremitalpa namibensis*). *J. Zool.* **244**, 107–117 (1998).
75. E. R. Trueman, The dynamics of burrowing in *Ensis* (Bivalvia). *Proc. R. Soc. Lond. B Biol. Sci.* **166**, 459–476 (1967).
76. B. D. Texier, A. Ibarra, F. Melo, Low-resistive vibratory penetration in granular media. *PLOS ONE* **12**, e0175412 (2017).
77. M. Alsaydalani, C. Clayton, Internal fluidization in granular soils. *J. Geotech. Geoenviron. Eng.* **140**, 04013024 (2014).
78. D. Firstbrook, K. Worrall, R. Timoney, F. Suñol, Y. Gao, P. Harkness, An experimental study of ultrasonic vibration and the penetration of granular material. *Proc. R. Soc. A Math. Phys. Eng. Sci.* **473**, 20160673 (2017).
79. D. Pachisia, E. Quinn, B. Shitaye, J. Wang, “Soft eversion robots in application of minimally invasive subsurface drip irrigation,” thesis, Princeton University, Princeton, NJ (2020).
80. E. Bierhaus, B. Clark, J. Harris, K. Payne, R. Dubisher, D. Wurts, R. Hund, R. Kuhns, T. Linn, J. Wood, The OSIRIS-REx spacecraft and the touch-and-go sample acquisition mechanism (TAGSAM). *Space Sci. Rev.* **214**, 107 (2018).
81. A. Van Burkalow, Angle of repose and angle of sliding friction: An experimental study. *Geol. Soc. Am. Bull.* **56**, 669–707 (1945).

Funding: This work is supported by the NSF (grant nos. 1637446, 1915445, 1915355, and 1935548), the Army Research Office (grant no. GR10005043), the Packard Foundation, and by an Early Career Faculty grant from NASA’s Space Technology Research Grants Program. The work of N.D.N. is supported by a NASA Space Technology Research Fellowship. **Author contributions:** N.D.N. designed the robot, wrote the manuscript, prepared videos, and performed experiments. A.K. prepared figures and performed experiments. M.M.-C., Y.O.-A., and E.A. performed experiments. D.I.G. advised the paper and experiments. E.W.H. advised the design of robot, wrote the manuscript, and advised the paper and experiments. **Competing interests:** N.D.N. and E.W.H. are authors of international patent application WO2020060858A1, related to this work. All other authors declare that they have no competing interests. **Data and materials availability:** All data needed to evaluate the conclusions in this paper are present in the paper and the Supplementary Materials.

Submitted 14 August 2020

Accepted 21 May 2021

Published 16 June 2021

10.1126/scirobotics.abe2922

Citation: N. D. Naclerio, A. Karsai, M. Murray-Cooper, Y. Ozkan-Aydin, E. Aydin, D. I. Goldman, E. W. Hawkes, Controlling subterranean forces enables a fast, steerable, burrowing soft robot. *Sci. Robot.* **6**, eabe2922 (2021).

Controlling subterranean forces enables a fast, steerable, burrowing soft robot

Nicholas D. Naclerio, Andras Karsai, Mason Murray-Cooper, Yasemin Ozkan-Aydin, Enes Aydin, Daniel I. Goldman and Elliot W. Hawkes

Sci. Robotics **6**, eabe2922.
DOI: 10.1126/scirobotics.abe2922

ARTICLE TOOLS

<http://robotics.sciencemag.org/content/6/55/eabe2922>

SUPPLEMENTARY MATERIALS

<http://robotics.sciencemag.org/content/suppl/2021/06/14/6.55.eabe2922.DC1>

RELATED CONTENT

<http://robotics.sciencemag.org/content/robotics/6/55/eabj3949.full>
<http://robotics.sciencemag.org/content/robotics/2/8/eaan3028.full>

REFERENCES

This article cites 56 articles, 6 of which you can access for free
<http://robotics.sciencemag.org/content/6/55/eabe2922#BIBL>

PERMISSIONS

<http://www.sciencemag.org/help/reprints-and-permissions>

Use of this article is subject to the [Terms of Service](#)

Science Robotics (ISSN 2470-9476) is published by the American Association for the Advancement of Science, 1200 New York Avenue NW, Washington, DC 20005. The title *Science Robotics* is a registered trademark of AAAS.

Copyright © 2021 The Authors, some rights reserved; exclusive licensee American Association for the Advancement of Science. No claim to original U.S. Government Works

Supplementary Materials for
Controlling subterranean forces enables a fast, steerable, burrowing soft robot

Nicholas D. Naclerio *et al.*

Corresponding author: Nicholas D. Nacleiro, nnaclerio@ucsb.edu

Sci. Robot. **6**, eabe2922 (2021)
DOI: 10.1126/scirobot.abe2922

The PDF file includes:

Experimental methods
Derivation of critical length for self-anchoring
Figs. S1 to S9

Other Supplementary Material for this manuscript includes the following:

Movies S1 to S6

Supplementary Materials

Experimental Methods

Force Arrows in Fig. 1A Forces were calculated for a 1 cm diameter, 1 cm long steel cylinder moving horizontally at 4 m/s through air, water, and 8 cm deep dry sand. Air and water drag forces were calculated using the fluid dynamics drag equation. The drag force in sand was interpolated from the experimental results in Fig. 6B, and the lift force was calculated from the lift to drag ratio found in the results in Fig. 4 without air flow.

Horizontal Tip Extension Experiment in Fig. 2 Experiments were performed in a 70x90x35 cm³ bed (Fig. S7) of dry silica sand (polydisperse particles ranging in diameter from 300 to 850 microns, Cemex Lapis Lustre 30 Mesh Sand). The bed was fluidized for 3 seconds between trials by blowing compressed nitrogen through an inlet at the bottom of the bed for a repeatable initial condition with an approximate volume fraction of 58%. An everting robot with a 22 mm diameter was positioned horizontally under a depth of 8 cm of sand, entering the bed through a tube in its side. The tip started 26 cm into the bed to reduce boundary affects from the bed inlet. The robot was grown 60 cm horizontally through the sand along a pre-tensioned steel wire that spanned the container to maintain a constant depth. The body pressure was recorded by an SSI Technologies digital pressure gauge and multiplied by its cross sectional area to approximate growing force. The pressure of the robot was slowly increased until it grew 4 cm. Growth was stopped and the pressure was manually recorded. This process was repeated until the robot grew approximately 60 cm for four trials. The test was repeated at the same depth with a rigid intruder of identical dimensions, built from a 21 mm diameter PVC tube sheathed in the skin of the everting robot, recording intrusion force with a Nextech DFS200 force gauge.

Vertical Intrusion Experiments in Figure 3 Experiments were performed in a 42x28x15 cm³ bed (Fig. S5) of dry silica sand (polydisperse particles ranging in diameter from 425 to 850 microns with a friction angle of 36° with a corresponding overall coefficient of friction of 0.72, Quikrete Filter Sand). Between each trial, the bed was fluidized by blowing air from the bed's bottom inlet for 15 seconds to repeatably reset the sand to a loosely consolidated initial condition with an approximate volume fraction of 58%. Experiments were performed by a DENSO VS087 robot arm connected to a 6-axis ATI Mini40 force/torque transducer controlled by a National Instruments DAQ running LabView. A tool transformation was used to calculate the forces on the face of the intruder from the force and torque data recorded by the sensor. All intruding bodies were 3D printed from ABS plastic using a Dimension Elite printer. The air flow rates were recorded by an Omega FMA1845 mass flowmeter, and controlled by an ARO pressure regulator.

In the vertical intrusion tests, the intruder was a 27 mm diameter, 100 mm tall cylinder with a 10 mm diameter circular opening at the bottom for airflow. It was attached to the force transducer with a 13 mm thick, 100 mm long steel shaft (Fig. S5A). Air flow was initialized as the intruder touched the surface of the sand, and was lowered at 10 mm/s for three trials at each flow rate. Power was calculated as the pressure of air flow at the base of the intruder times volumetric flow rate.

Horizontal Intrusion Experiments in Fig. 4 These tests used the identical setup as the vertical tests but with a different intruder tip. The horizontal intruder was a 30 mm diameter, 30 mm long cylinder with its flat surface facing the direction of drag (Fig. S5B). For each tested angle of tip air flow, we used a different intruder with identical external dimension and an 8 mm diameter hole for airflow at 15 degree increments from the horizontal of the cylinder's center of geometry. The intruder was first lowered into the fluidized sand bed, then bed fluidization was

turned off and the sand left to settle, then tip-based air flow was turned on and the intruder was dragged horizontally. Four trials were conducted for each flow and angle condition at a depth of 43 mm. We reported the average steady state resistive force, which occurs after one or two body lengths of movement. Only one trial was conducted at 80 mm, so we report the average and standard deviation of the steady state force of that one trial. Raw data for that test is available in Fig. S9. The reaction force of the air flow jet without sand has not been subtracted from the results. The control lines plotted in Fig. 4 are the average force measured on an intruder without a hole for tip flow. The force on the steel rod moving horizontally through sand without a tip or air flow was subtracted from the results. Although the forces on the rod may be different with air flow, due to the increasing lithostatic pressure, the shallow rod has substantially less drag force than the deeper intruder tip.

Characterization of Robot Anchoring Experiments in Fig. 5 These tests were performed with a similar setup and procedure as the experiment in Fig. 2. To test pull out force, the 22 mm diameter robot with a constant pressure of 30 kPa was pulled out by its body 4 cm at a time, recording the maximum tension required for three trials. The retraction force test was similar, measuring the force to retract the robot by its tail with a constant pressure of 30 kPa for three trials. The force gauge was used to measure the rejection force of the robot as it grew horizontally into the sand, recording the maximum reaction force for every 4 cm increment for three trials. The force gauge was mounted one end to the inlet tube of the sand bed, and attached at the other end to the robot body on the outside of the sand bed.

Internal Pressure vs. Flow Rate Experiment in Fig. 6A This experiment was performed with the full sized robot described in the Robot Design and Robot Fabrication sections. The robot was placed inside the sand box via the side entrance tube with a depth of 8 cm of sand above it. For various downward air flow rates, measured with a Brooks Instruments 10 SCFM

variable area flow meter, the maximum pressure required to grow 1 cm was recorded with the pressure transducer. Five tests were recorded at each flow rate.

High Speed Growth Rate Experiments in Fig. 6B The growth rate experiment in Fig. 6B was performed with the same robot setup as above. The body pressure was suddenly turned on for one second by manually opening a ball valve, allowing the robot to grow without constraint. The maximum reaction force was recorded by the force gauge. As the robot passed through the sand, it disturbed three rows of upright matchsticks spaced 20 cm apart on the surface of the sand (note that they are only spaced 15 cm apart in the demonstration in Fig. 6C) The speed of the robot was calculated by recording the disturbance of surface sand and match sticks as the robot grew (iPhone 7 240 fps video). One test was performed at six different pressures.

Downward Flow rate vs. Robot Trajectory Experiment in figures 6D,E,F Identical experimental setup as above, but with an 8 mm wide, 2 mm thick, 20 cm long carbon fiber mast with depth markings every 2 cm attached to the air flow tip to track the position of the robot. With a body pressure of 100 kPa, the robot burrowed at approximately 2 cm/s over 60 cm horizontally with various rates of downward air flow. The position of the mast was recorded by video (iPhone 7), and the approximate linear trajectory of the robot was estimated by the initial and final mast depths. One trial at each of six flow rates was recorded.

Robot Steering Demonstrations in Fig. 7 Identical experimental setup as above for horizontal steering demos in Fig.7A,B,C. With a body pressure of approximately 100 kPa and a downward air flow rate of up to 300 L/min, the robot burrowed horizontally through the sand under a depth of 8 cm of sand. The right hand turn in Fig. 7B and C was initiated by applying a displacement of 65 mm to the right side steering tendon before growing the robot. As the robot grew, the tendon displacement remained fixed. To initiate the left turn in Fig. 7 C, the growth

of the robot was stopped, the tension on the right side tension was released, a displacement of 65 mm was added to the left side tendon, and the robot was allowed to grow again around the wooden obstacle.

The vertical steering demonstrations in Fig. 7D and E were performed in a 70x8x35 cm sand bed with a clear glass and acrylic side panel. With a body pressure of approximately 100 kPa and a forward air flow rate of approximately 30 L/min, the robot was able to burrow vertically. To steer under the obstacle in Fig. 7E, a downward air flow rate of approximately 100 L/min was added as the robot transitioned from a vertical to horizontal orientation. The turn was achieved by displacing the top steering tendon over 65 mm.

The demonstration in Fig. 7F was performed with a 6 cm diameter robot body, sewn from X-Pac TX07 fabric (Rockywoods) and sealed with 0.51DCF Dyneema composite fabric (Ripstop by the Roll) and a pressure sensitive adhesive (3M 9482PC). The robot had an identical tip-based flow device as described above, with a preshaped turn sewn into its body. With a body pressure of approximately 200 kPa and a combined downward and forward air flow rate of approximately 300 L/min the robot burrowed down, under, and up on the other side of a 20 cm thick cinder block wall buried 15 cm deep.

Rate Dependence Experiments in Fig. S3 These experiments were performed in a 18x18x60 cm³ bed filled with ~1 mm diameter poppy seeds. Poppy seeds were used instead of sand, because the robot is not strong enough to penetrate vertically into sand without air flow. Between each trial the bed was fluidized by blowing air from its bottom inlet to create a repeatable loose packed initial condition. The setup consisted of a 6-axis ATI Mini40 force/torque sensor attached to an aluminum frame on the top of the bed, two Nema17 stepper motors, an Arduino Uno control board, a pressure sensor (Honeywell, *HSCDANN015PAAA5*), an X-ray machine (Orthoscan DI Mini C-arm) and air supply (Fig. S6A). An everting robot with a 4 cm diameter

was attached to a custom connector below the force sensor (Fig. S6B). The growth rate of the robot was controlled by the two growth control wires (yellow Kevlar thread in Fig. S6B) which were connected between the stepper motors and the tail of the robot.

The robot was grown into the granular media with a constant body pressure of 34.5 kPa at three different growth rates (0.4, 0.6 and 0.8 cm/s, driven by stepper motors) starting from 1.5 cm above the surface of the granular media. A metal strip attached to the center-line of the robot was visible in X-ray as it extended. A custom Labview program and NI USB-6216 DAQ device collected synchronized force, pressure and X-ray data (S6C). The growth rate of the robot was captured from frames of X-ray videos using the Matlab Image Analysis Toolbox. A synchronized webcam recorded the tip position above the granular media. At each growth speed, we did four experiments and plot the average normal force vs. growth length in Fig. S3.

Robot Steering Characterization Experiment in Fig. S4 Tests were conducted with the full sized robot as described in the Robot Fabrication section in air, in sand without tip flow, and in sand with tip flow. For repeatable testing, the tendon housing was opened, inspected, and cleaned of any sand between trial sets. Trials in sand began at depth of 8 cm, although the trials without air flow surfaced. Three sets of trials were conducted, each one testing in each medium once. Each trail set began in a different medium. For each trial, one steering tendon was displaced 65 mm to create an average radius of curvature of 46 cm.

Derivation of critical length for self anchoring Self anchoring occurs when the tangential forces due to friction along the length of the robot body exceed the normal forces at its tip (Fig. S8). This means that after a certain length, the robot requires no reaction force at the base prevent the robot from being ejected from the ground by reaction forces.

The friction forces can be approximated as

$$F_{friction} = \mu N = \mu P(h) A_{body} \quad (1)$$

where μ is the coefficient of friction between the robot and its environment, N is the normal force applied on the body, $P(h)$ is the external pressure as a function of depth h , and A is the surface area. Assuming that the shape of the robot is a cylinder with radius r , and length L this becomes

$$F_{friction} = \mu P(h) 2\pi r L. \quad (2)$$

Similarly, the normal force applied at the tip of the robot can be written as

$$F_{normal} = P(h) A_{tip} = P(h) \pi r^2. \quad (3)$$

If we make the simplifying assumption that $P(h)$ is due only to lithostatic pressure, when the robot is moving horizontally, $P(h)$ experienced on the tip and sides of the robot is the same. When it is burrowing vertically down, and we assume a linearly increasing lithostatic pressure, the average $P(h)$ on the sides is half that at the tip. In reality, the force on the tip of the robot is even higher than this assumption, because the tip must overcome some resistive strength that the sides do not. Further, cohesion may reduce the pressure exerted on the sides of the robot (as found by the HP³ probe (23)). Thus, the robot self anchors at a length at least L_{anchor} when (2) equals (3). Therefore, only considering forces in the direction of motion in horizontal burrowing:

$$L_{anchor} > \frac{r}{2\mu} (\text{horizontal}) \quad (4)$$

and in vertical burrowing:

$$L_{anchor} > \frac{r}{\mu} (\text{vertical}). \quad (5)$$

Supplementary Figures

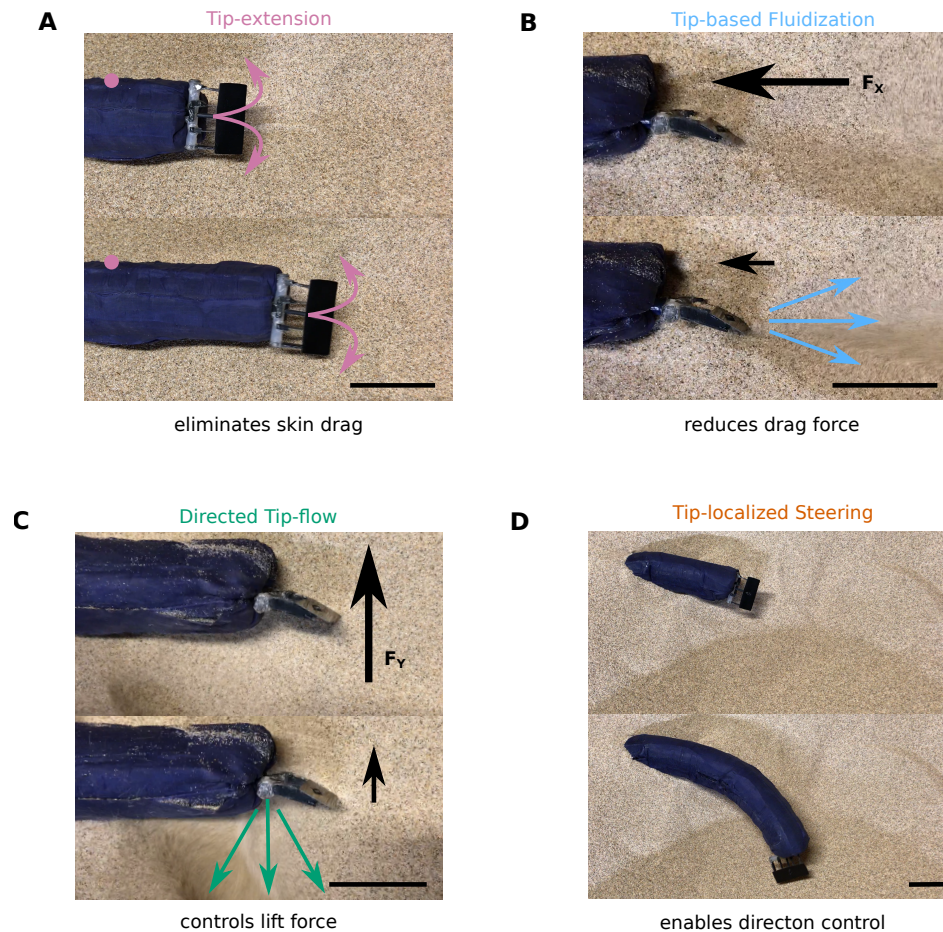


Figure S1: Photos of the robot's primary features. (A) Tip extension allows the robot body to remain stationary as new material is added to the tip through eversion (pink dot remains stationary as tip extends, see Movie S1). (B) Tip-based air flow reduces drag by decreasing the strength of the surrounding media (see Movie S2). (C) Directed tip flow allows the robot to control lift (see Movie S2). (D) Tip extension and tip-localized steering enable controlled subterranean steering in sand in both the horizontal and vertical planes (see Fig. 7 and Movies S3 and S4). Scale bars are all 6 cm, the diameter of the robot.

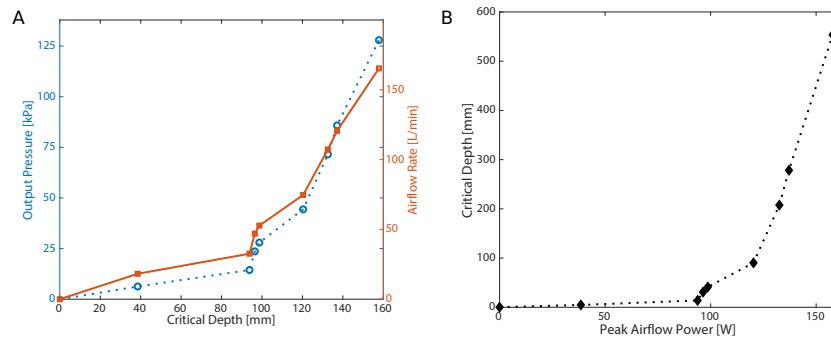


Figure S2: **Tip-based air pressure, flow rate, and power as a function of critical depth.** Critical depth is defined as when the force during intrusion with air flow reaches 30% of the force required without air flow (see Fig. 3). Power is approximated as pressure times volumetric flow rate. N=3 trials.

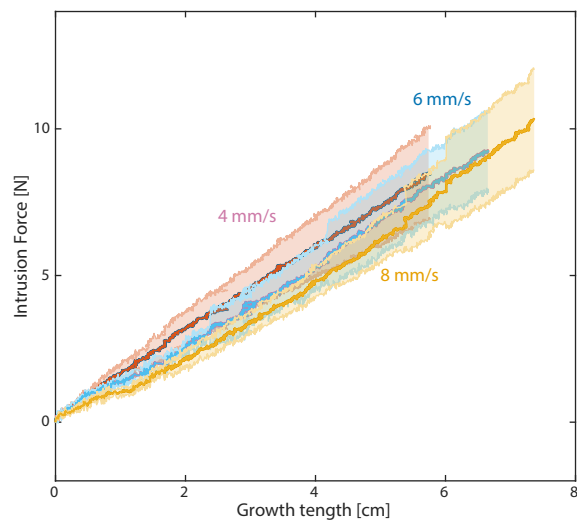


Figure S3: **Growth rate vs. intrusion force.** Intrusion force remains roughly constant at low growth rates in vertical burrowing in poppy seeds without air flow. N=4 trials. Error bars denote plus/minus one SD.

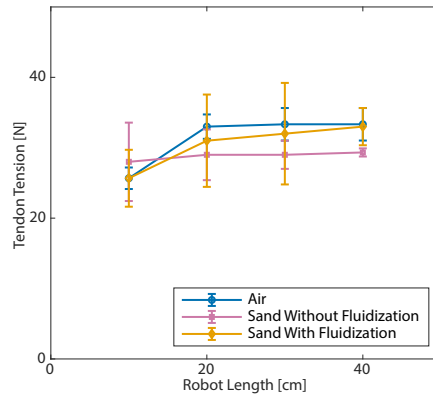


Figure S4: **Steering tendon tension vs. length when turning.** Test conducted in air, sand without air flow, and sand with air flow. The robot lengthened under a constant tendon displacement, radius of curvature, and body pressure. N=3 trials. Error bars denote plus/minus one SD.

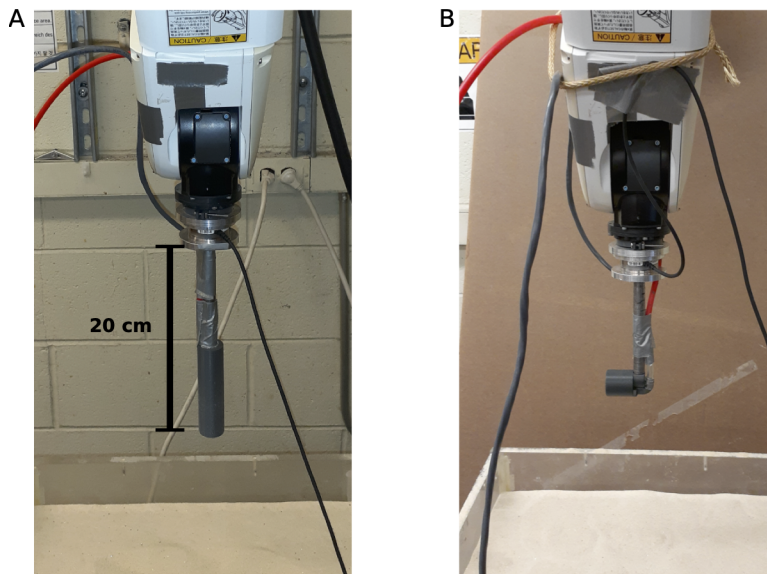


Figure S5: **Experimental setup used for horizontal lift and drag experiments.** (A) The vertical intruder is mounted on a force torque sensor on a robot arm. It was plunged vertically 15 cm into the sand with varying levels of air flow rate. (B) The horizontal intruder is mounted on the same setup. It was dragged horizontally through the sand while measuring lift and drag forces with varying air flow rates and direction.

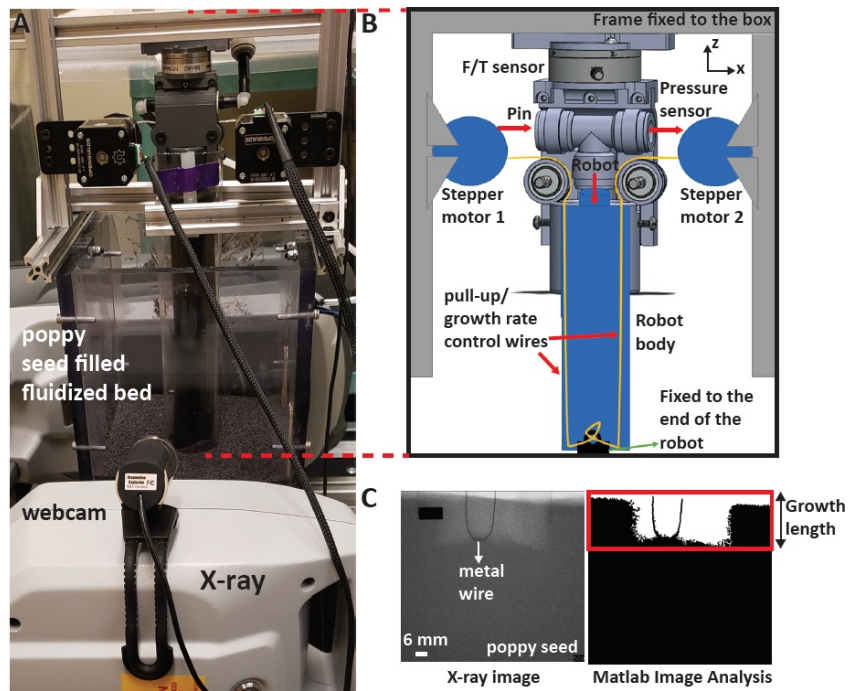


Figure S6: **Growth rate vs. intrusion force experimental setup.** (A) The setup including force/torque sensor, everting robot, poppy seed filled bed, and X-ray machine. (B) Details of the rate control mechanism shown in A. (C) A frame of X-ray video showing the position of the robot's centerline under poppy seeds (left). An example X-ray image processed by Matlab's Image Processing toolbox (right).



Figure S7: **Robot characterization experimental setup.** The sand bed is split into two sections, one open bed for horizontal burrowing (70x90x35 cm), and one narrow bed with a glass side for vertical burrowing visualization (70x8x35 cm). The depressurized robot (purple, with grey tip-based air supply line, white pressurization tube, and white tail string) can be seen entering the sand bed through an inlet pipe on the left side of the bed. The bed can be fluidized by the compressed nitrogen tank on the right.

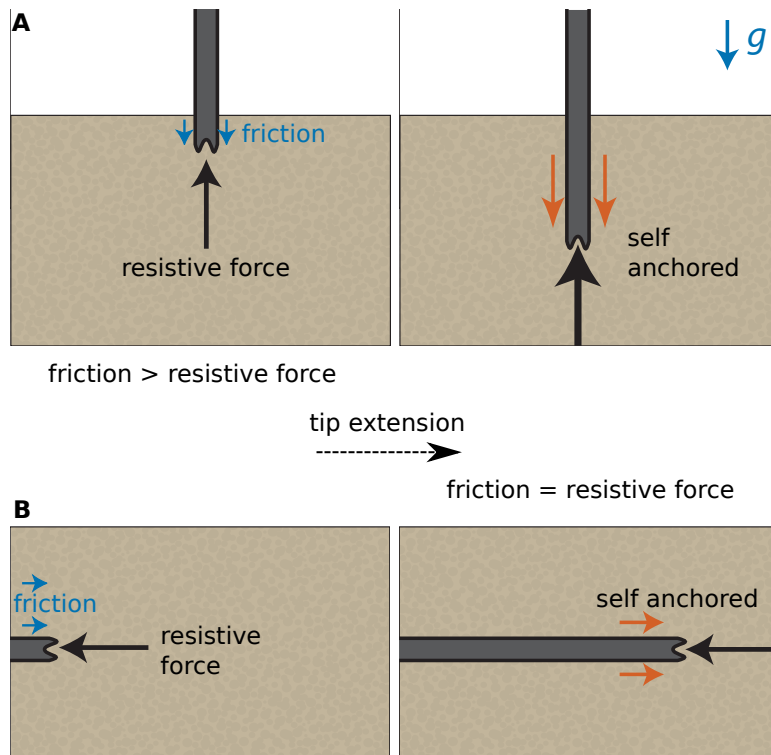


Figure S8: **Self Anchoring Force Balance** (A) When friction forces and reaction forces on a vertically-burrowing tip-extending robot balance each other the robot is self-anchored. (B) When the forces balance each other in horizontal burrowing, the robot is also self anchored.

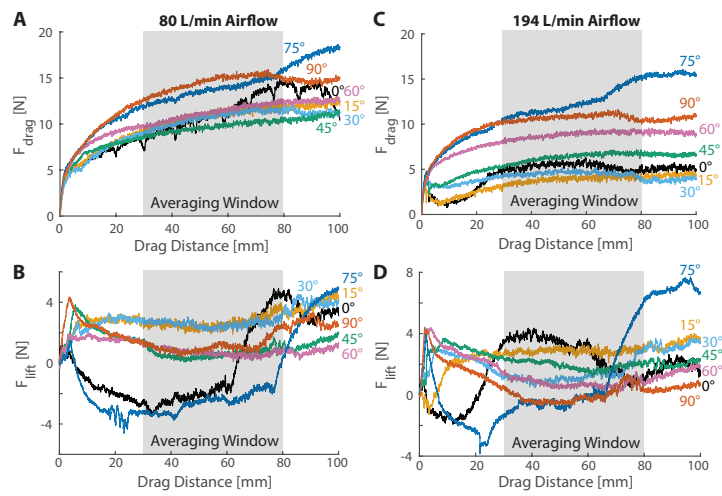


Figure S9: **Raw Data for 80 mm Depth Horizontal Intrusion Test** See Fig. 4C and E for steady state mean and standard deviation taken from a distance range of 30 mm to 80 mm. N=1 trial. **(A)** Drag force vs. intrusion distance as a function of tip flow angle with a flow rate of 80 L/min. **(B)** Drag force vs. intrusion distance as a function of tip flow angle with a flow rate of 194 L/min. **(C)** Lift force vs. intrusion distance as a function of tip flow angle with a flow rate of 80 L/min. **(D)** Lift force vs. intrusion distance as a function of tip flow angle with a flow rate of 194 L/min.